

# Strong yet ductile nanolamellar high-entropy alloys by additive manufacturing

<https://doi.org/10.1038/s41586-022-04914-8>

Received: 30 June 2021

Accepted: 27 May 2022

Published online: 3 August 2022

 Check for updates

Jie Ren<sup>1,9</sup>, Yin Zhang<sup>2,9</sup>, Dexin Zhao<sup>3</sup>, Yan Chen<sup>4</sup>, Shuai Guan<sup>1</sup>, Yanfang Liu<sup>1</sup>, Liang Liu<sup>1</sup>, Siyuan Peng<sup>1</sup>, Fanyue Kong<sup>1</sup>, Jonathan D. Poplawsky<sup>5</sup>, Guanhui Gao<sup>6</sup>, Thomas Voisin<sup>7</sup>, Ke An<sup>4</sup>, Y. Morris Wang<sup>8</sup>, Kelvin Y. Xie<sup>3</sup>, Ting Zhu<sup>2,✉</sup> & Wen Chen<sup>1,✉</sup>

Additive manufacturing produces net-shaped components layer by layer for engineering applications<sup>1–7</sup>. The additive manufacture of metal alloys by laser powder bed fusion (L-PBF) involves large temperature gradients and rapid cooling<sup>2,6</sup>, which enables microstructural refinement at the nanoscale to achieve high strength. However, high-strength nanostructured alloys produced by laser additive manufacturing often have limited ductility<sup>3</sup>. Here we use L-PBF to print dual-phase nanolamellar high-entropy alloys (HEAs) of AlCoCrFeNi<sub>2.1</sub> that exhibit a combination of a high yield strength of about 1.3 gigapascals and a large uniform elongation of about 14 per cent, which surpasses those of other state-of-the-art additively manufactured metal alloys. The high yield strength stems from the strong strengthening effects of the dual-phase structures that consist of alternating face-centred cubic and body-centred cubic nanolamellae; the body-centred cubic nanolamellae exhibit higher strengths and higher hardening rates than the face-centred cubic nanolamellae. The large tensile ductility arises owing to the high work-hardening capability of the as-printed hierarchical microstructures in the form of dual-phase nanolamellae embedded in microscale eutectic colonies, which have nearly random orientations to promote isotropic mechanical properties. The mechanistic insights into the deformation behaviour of additively manufactured HEAs have broad implications for the development of hierarchical, dual- and multi-phase, nanostructured alloys with exceptional mechanical properties.

Additive manufacturing often produces microstructures with highly heterogeneous grain geometries, subgrain dislocation structures and chemical segregation in metallic materials, including steels<sup>5,6</sup>, cobalt- or nickel-based superalloys<sup>8,9</sup>, aluminium alloys<sup>2</sup>, titanium alloys<sup>3,8,10</sup> and high-entropy alloys (HEAs)<sup>11</sup>. Eutectic HEAs (EHEAs) represent a promising class of multi-principal-element alloys (also called compositionally complex alloys)<sup>12,13</sup> that can form a hierarchical microstructure of dual-phase lamellar colonies and thus offer great potential for achieving excellent mechanical properties<sup>14</sup>. However, the thicknesses of lamellae are usually in the range of micrometres or submicrometres by conventional solidification routes, which limits the attainable strengths of these EHEAs<sup>14–16</sup>. By contrast, nanolayered and nanolamellar metals exhibit high strength but come at the expense of low ductility<sup>17,18</sup>. These materials have been fabricated through thin-film deposition<sup>19</sup> or severe plastic deformation<sup>18,20</sup>, which usually results in highly textured nanostructures with strong plastic anisotropy, limiting their practical applications. Here we harness the extreme printing conditions of laser

powder bed fusion (L-PBF) and the favourable compositional effects of HEAs to produce a unique type of far-from-equilibrium microstructure in the form of dual-phase nanolamellae embedded in eutectic colonies in an AlCoCrFeNi<sub>2.1</sub> EHEA (Fig. 1). This additively manufactured (AM) EHEA demonstrates an excellent combination of strength and ductility together with nearly isotropic mechanical behaviour.

Achieving a rational control of the solidification microstructures and defects in AM materials is challenging because of an intrinsically large parameter space of laser processing<sup>7</sup>. Using the normalized equivalent-energy-density method<sup>21</sup>, we identified an effective L-PBF processing window to print fully dense AlCoCrFeNi<sub>2.1</sub> EHEA samples (Supplementary Section 1). By adjusting the laser power and scan speed, we were able to reduce the lamellar thicknesses to tens of nanometres, as shown in the representative samples A and B (Supplementary Section 1). Despite their microstructural similarity, we focused on characterizing sample A with finer nanolamellae and used sample B to demonstrate the tunability of the nanolamellar structures and

<sup>1</sup>Department of Mechanical and Industrial Engineering, University of Massachusetts, Amherst, MA, USA. <sup>2</sup>George W. Woodruff School of Mechanical Engineering, Georgia Institute of Technology, Atlanta, GA, USA. <sup>3</sup>Department of Materials Science and Engineering, Texas A&M University, College Station, TX, USA. <sup>4</sup>Neutron Scattering Division, Oak Ridge National Laboratory, Oak Ridge, TN, USA. <sup>5</sup>Center for Nanophase Materials Sciences, Oak Ridge National Laboratory, Oak Ridge, TN, USA. <sup>6</sup>Rice Electron Microscopy Center, Department of Materials Science and Nano-Engineering, Rice University, Houston, TX, USA. <sup>7</sup>Materials Science Division, Lawrence Livermore National Laboratory, Livermore, CA, USA. <sup>8</sup>Department of Materials Science and Engineering, University of California, Los Angeles, CA, USA. <sup>9</sup>These authors contributed equally: Jie Ren, Yin Zhang. ✉e-mail: ting.zhu@me.gatech.edu; wenchen@umass.edu

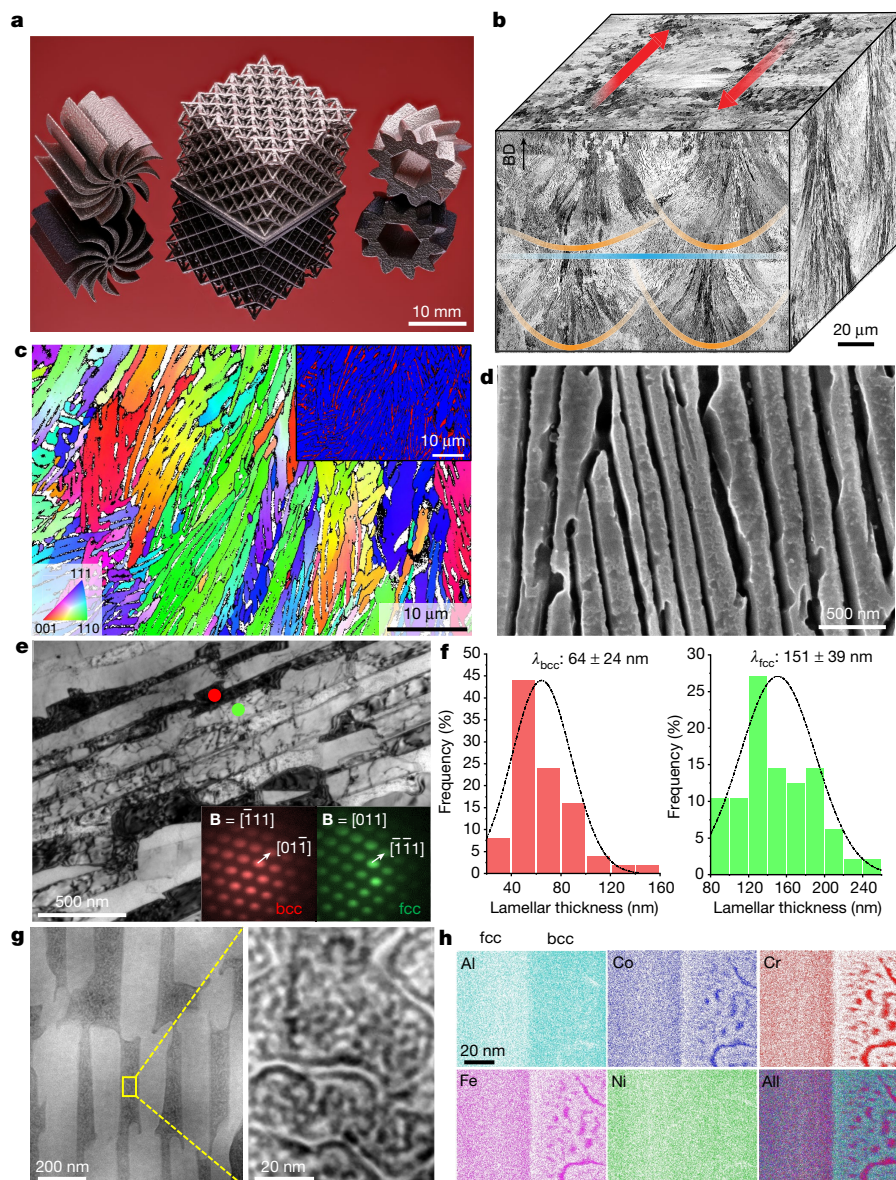


**Fig. 1 | Microstructure of AM AlCoCrFeNi<sub>2.1</sub> EHEA. a**, Printed heatsink fan, octet lattice (strut size of about 300  $\mu\text{m}$ ) and gear (from left to right). **b**, Three-dimensional reconstructed optical micrographs of as-printed AlCoCrFeNi<sub>2.1</sub> EHEA. The interlayer boundary, melt pool boundaries and laser scan tracks are illustrated by the blue line, orange lines and red arrows, respectively. The build direction (BD) is vertical. **c**, A cross-sectional EBSD IPF map of as-printed AlCoCrFeNi<sub>2.1</sub> EHEA, showing a magnified local region where neighbouring nanolamellar eutectic colonies exhibit different crystallographic orientations. To better display the finer bcc nanolamellae, the inset shows a two-colour EBSD phase map with fcc lamellae in blue and bcc lamellae in red. It is noted that the bcc nanolamellae are under-indexed owing to their small thicknesses close to the resolution limit of EBSD (see Supplementary Fig. 3

for the morphology of dual-phase nanolamellar eutectic colonies). **d**, Secondary electron micrograph of the nanolamellar structure. **e**, Bright-field TEM image of the bcc and the fcc nanolamellae (indicated by a red dot and a green dot, respectively), with the insets showing PED patterns tilted to the zone axes (**B**)  $[\bar{1}11]_{\text{bcc}}$  and  $[011]_{\text{fcc}}$ , respectively. **f**, Lamellar thickness distribution of the bcc (left) and the fcc (right) lamellae in as-printed AlCoCrFeNi<sub>2.1</sub> EHEA.

**g**, HAADF-STEM image showing the modulated nanostructures within bcc lamellae. **h**, APT maps of elemental distribution in a  $100 \times 78 \times 5 \text{ nm}^3$  section with an fcc/bcc interface in the centre. Chemical fluctuations within bcc lamellae are manifested by the nanoscale Ni–Al-rich and Co–Cr–Fe-rich regions. The compositions of dual phases are extracted from one-dimensional concentration profile analysis and are listed in Extended Data Table 1.

associated properties. In addition, we printed a variety of representative engineering components, including a heatsink fan, an octet-truss microlattice and a gear (Fig. 1a), which demonstrate the excellent printability of this EHEA for a wide range of complex geometries.

A hierarchical microstructure is realized in the as-printed AlCoCrFeNi<sub>2.1</sub> EHEA, which features dual-phase nanolamellar eutectic colonies (Fig. 1b–d). These eutectic colonies exhibited elongated shapes with typical sizes of 20–30  $\mu\text{m}$  and 2–6  $\mu\text{m}$  along the long and short axes, respectively (Fig. 1c). Elongated colonies associated with a melt pool

were largely aligned with the direction of the maximum local thermal gradient perpendicular to the melt pool boundary<sup>22</sup>, which exhibited an approximately semicircular shape (Fig. 1b and Supplementary Fig. 3 in Supplementary Section 2). As a result, these elongated colonies were oriented towards the centre of the melt pool, leading to almost random shape orientations. There were also markedly different crystallographic orientations between neighbouring colonies (Fig. 1c). The nearly random orientations in the shape and the crystallography of the eutectic colonies probably originate from the interplay between competitive

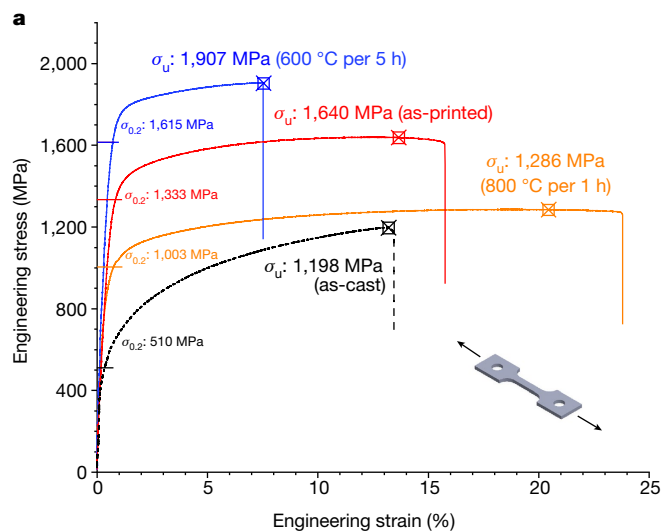
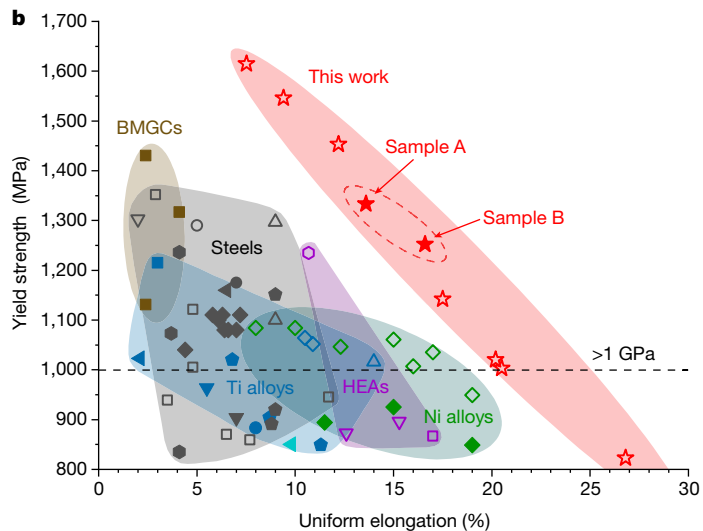


**Fig. 2 | Tensile properties of AM AlCoCrFeNi<sub>2.1</sub> EHEAs. a**, Tensile stress–strain curves of as-printed and annealed AlCoCrFeNi<sub>2.1</sub> EHEAs. The yield strength ( $\sigma_{0.2}$ ) and ultimate tensile strength ( $\sigma_u$ ) are marked on the curves. The inset shows the schematic of a dogbone-shaped specimen under tensile loading. **b**, Tensile yield strength versus uniform elongation of AM AlCoCrFeNi<sub>2.1</sub> EHEAs compared with those of high-performance AM metal alloys with high strength



( $\sigma_{0.2} > 800$  MPa) in the literature, including bulk metallic glass composites (BMGCs), steels, Ni-based superalloys, titanium (Ti)-based alloys and HEAs. The solid and hollow symbols represent the properties of as-printed and post-annealed samples, respectively (see the detailed data, symbol description and associated references in Supplementary Table 5).

growth owing to site-specific thermal schedules (dictated by laser beam size, energy density input and so on) and epitaxial growth owing to partial remelting of previously deposited layers. In addition, the scan strategy of 90° rotation between adjacent layers can perturb heat fluxes, further promote random orientations of eutectic colonies<sup>22</sup> and thus suppress texture formation (Extended Data Fig. 1). No appreciable changes in chemical composition were observed between the feeding AlCoCrFeNi<sub>2.1</sub> powders and the as-printed samples (Supplementary Table 2). Within these eutectic colonies, the formation of dual-phase nanolamellae is facilitated by high cooling rates of 10<sup>5</sup>–10<sup>7</sup> K s<sup>-1</sup> associated with L-PBF<sup>1</sup>. Scanning electron microscopy (SEM) and transmission electron microscopy (TEM) characterizations revealed dual-phase nanolamellae consisting of alternating body-centred cubic (bcc) and face-centred cubic (fcc) nanolayers (Fig. 1d,e), with respective thickness of  $\lambda_{\text{bcc}} = 64 \pm 24$  nm and  $\lambda_{\text{fcc}} = 151 \pm 39$  nm (Fig. 1f). The corresponding interlamellar spacing is  $\lambda \approx 215$  nm, which is approximately half of that in the starting powder feedstock (Supplementary Fig. 4). Such dual-phase nanolamellar structures are in contrast to the typical dual-phase microlamellar structures of EHEAs from conventional casting ( $\lambda \approx 0.77$ –5  $\mu\text{m}$ )<sup>14,23</sup>, directional solidification ( $\lambda \approx 2.8$   $\mu\text{m}$ )<sup>16</sup> or thermomechanical treatment ( $\lambda \approx 1$ –5  $\mu\text{m}$ )<sup>23,24</sup>. The much thinner nanolamellae in our AM EHEA are understandably a result of rapid solidification from L-PBF.

The AlCoCrFeNi<sub>2.1</sub> EHEA from L-PBF shows distinct elemental distributions and phase structures compared with conventional counterparts<sup>14,23–25</sup>. Both the fcc and the bcc phases in as-printed samples are solid solutions, as seen by the absence of extra superlattice spots in the precession electron diffraction (PED) patterns (Fig. 1e). A classical Kurdjumov–Sachs orientation relationship was identified between the fcc and the bcc phases, giving  $\{111\}_{\text{fcc}} \parallel \{110\}_{\text{bcc}}$  and  $\langle 110 \rangle_{\text{fcc}} \parallel \langle 111 \rangle_{\text{bcc}}$  (ref. 26). Compositional analyses by atom probe tomography (APT) revealed marginal chemical segregations between the dual phases (Extended Data Table 1). Neutron-diffraction measurements confirmed that the as-printed EHEA is composed of fcc and bcc solid solutions, which have a weight fraction of 67% and 33%, respectively, and a lattice mismatch of 2.3% (Supplementary Section 3). No precipitates were detected in the as-printed samples. In contrast, the conventional AlCoCrFeNi<sub>2.1</sub> EHEAs consist of ordered L1<sub>2</sub> and B2 phases with

substantially different chemical compositions as well as copious nanoprecipitates; the B2/bcc lamellae are prominently rich in nickel (Ni) and aluminium (Al), whereas the L1<sub>2</sub>/fcc lamellae are highly enriched by cobalt (Co), chromium (Cr) and iron (Fe)<sup>14,23–25</sup>. The distinct lamellar thicknesses and elemental distributions between the AM and conventional AlCoCrFeNi<sub>2.1</sub> EHEAs indicate that atomic diffusion and chemical ordering are largely suppressed during rapid solidification of L-PBF. This is because with an increasing solidification rate, conventional diffusion-mediated solidification is shifted towards diffusion-limited solidification, leading to significantly reduced elemental partitioning in the dual-phase eutectic nanolamellae from L-PBF.

Compositional modulation at the nanoscale was found inside the bcc nanolamellae, which comprised two types of intertwined region with different contrast from high-angle annular dark-field scanning TEM (HAADF-STEM) imaging (Fig. 1g). APT and STEM energy dispersive X-ray spectroscopy (STEM-EDX) mapping revealed the bicontinuous Ni–Al rich and Co–Cr–Fe-rich nanostructures within the bcc nanolamellae (Fig. 1h and Supplementary Fig. 5). High-resolution TEM (HRTEM) imaging and the corresponding fast Fourier transform (FFT) diffractogram showed a consistent bcc lattice structure in these compositionally modulated regions (Extended Data Fig. 2), suggesting the occurrence of spinodal decomposition<sup>27</sup>. Such nanoscale compositional modulation has not been reported in conventional AlCoCrFeNi<sub>2.1</sub> EHEAs, underscoring the ability of additive manufacturing to produce highly metastable microstructures. Modulated chemical inhomogeneity can have an important role in the mechanical behaviour of HEAs<sup>28</sup>. Altogether, the extreme solidification conditions of L-PBF produce a hierarchical microstructure with a high degree of metastability (Extended Data Fig. 3).

The AM AlCoCrFeNi<sub>2.1</sub> EHEAs have exceptional mechanical properties compared with as-cast counterparts. The as-printed sample exhibits a high 0.2%-offset tensile yield strength of  $\sigma_{0.2} = 1,333 \pm 38$  MPa, which is substantially higher than  $510 \pm 15$  MPa of the as-cast sample (Fig. 2a). It also shows high rates of strain hardening at high flow stresses (Extended Data Fig. 4), leading to a large uniform elongation of about 14% and a corresponding ultimate tensile strength of  $\sigma_u = 1,640 \pm 38$  MPa. The sample after tensile rupture shows ‘cup and cone’ fracture surfaces with micro-dimples (Supplementary Fig. 6), which is indicative of ductile failure. The interlamellar spacing of our EHEA can be tailored

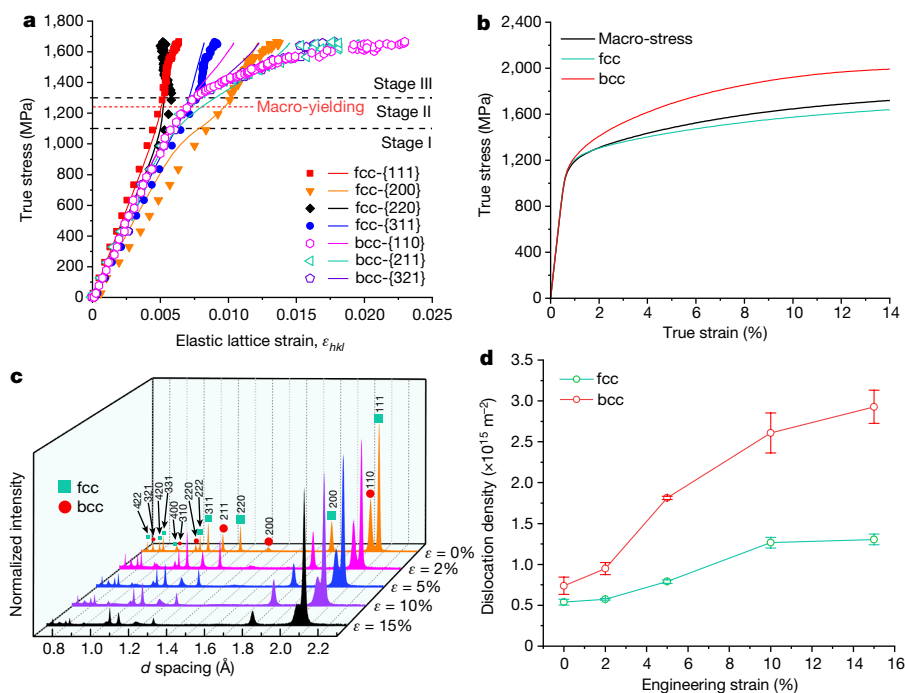


**Fig. 3 | Lattice strains and stress partitioning in fcc and bcc phases during uniaxial tension.** **a**, Evolution of lattice strain against macroscopic true stress for representative fcc (including {111}, {200}, {220} and {311}) and bcc (including {110}, {211} and {321}) crystallographic plane families along the loading direction. Experimental and simulation results are represented by symbols and solid lines, respectively. The macroscopic yield strength is marked with the red dashed line. **b**, DP-CPFE simulation results of the macroscopic stress–strain

response with the corresponding stress partitioning in the bcc and the fcc phases. **c**, Neutron-diffraction spectra at different tensile strains ( $\epsilon$ ) along the loading direction during deformation. **d**, Dislocation density against strain in the bcc and the fcc phases, derived from the diffraction spectra in **c** and the modified Williamson–Hall method (Supplementary Section 3). Error bars represent the standard deviation.

by varying the laser processing parameters to tune their mechanical properties, as exemplified by sample B (Fig. 2b and Supplementary Section 1). With a given laser processing scheme, similar mechanical properties were measured along the vertical and horizontal directions (Extended Data Fig. 5). This result demonstrates the nearly isotropic mechanical behaviour of as-printed AlCoCrFeNi<sub>2.1</sub> nanolamellar eutectic colonies with nearly random orientations in shape and crystallography, which are different from the anisotropic mechanical behaviour of highly aligned lamellar structures produced by other routes such as thermomechanical treatment<sup>18,24</sup> and directional solidification<sup>16</sup>. The mechanical isotropy of AM EHEAs is also in contrast to the typical mechanical anisotropy of other AM metal alloys that tend to develop columnar-shaped grain structures with a strong crystallographic texture<sup>1</sup>. In addition, subsequent heat treatment allowed us to further tailor microstructures and associated mechanical properties (Fig. 2b). For example, after thermal annealing at 800 °C for 1 h, a uniform elongation over 20% with a yield strength of about 1 GPa was achieved; after annealing at 600 °C for 5 h, the yield strength and ultimate tensile strength were increased to approximately 1.6 GPa and 1.9 GPa, respectively, along with a uniform elongation of 7.5%. Achieving such a wide range of strength–ductility combinations was facilitated by the high tunability of microstructures in rapidly solidified EHEAs through post annealing, during which a variety of solid-state phase transformations such as precipitation, phase ordering, lamellar coarsening and recrystallization could occur (Supplementary Section 4). Direct comparison of the tensile properties of our AM EHEAs with other high-performance AM alloys ( $\sigma_{0.2} > 800$  MPa) is given in Fig. 2b and Supplementary Section 5. Clearly, our AM EHEAs demonstrate excellent strength–ductility combinations that surpass those of state-of-the-art AM alloys.

The high yield strength (about 1.3 GPa) of our as-printed EHEA stems primarily from the strong strengthening effects of the dual-phase

nanolamellar structures. The alternating bcc and fcc nanolamellae with average thicknesses of 64 nm and 151 nm, respectively, together with their semi-coherent interfaces, can impose strong mutual confinement on dislocation glide<sup>20,26</sup>. Such nanolamellar strengthening gives a contribution of about 1 GPa to the yield strength, as estimated from the Hall–Petch relation (Methods)<sup>26</sup>. In addition, rapid solidification from L-PBF produces a high density of pre-existing dislocations in as-printed samples<sup>6</sup>, thus giving an extra strengthening effect. We used neutron-diffraction measurements to determine the pre-existing dislocation density in as-printed samples (Fig. 3 and Supplementary Section 3). The average dislocation densities in the bcc ( $\rho_{bcc}$ ) and the fcc ( $\rho_{fcc}$ ) nanolamellae reached as high as  $(7.4 \pm 1.1) \times 10^{14} \text{ m}^{-2}$  and  $(5.4 \pm 0.3) \times 10^{14} \text{ m}^{-2}$ , respectively, resulting in an estimated increase in yield strength of about 280 MPa (Methods). Hence, the high yield strength of our as-printed EHEA is enabled by the dual-phase nanolamellar structures from L-PBF and further enhanced by the high density of printing-induced dislocations.

The origin of high strain hardening and the resultant large tensile ductility of our as-printed EHEA were investigated by combining in situ neutron-diffraction experiments (Supplementary Fig. 8) with dual-phase crystal plasticity finite-element (DP-CPFE) modelling (Supplementary Section 6). In situ neutron-diffraction measurements under tension revealed the evolution of lattice strains in different {hkl} crystallographic families of fcc and bcc phases in nanolamellar eutectic colonies. Figure 3a shows the lattice strain  $\epsilon_{hkl}$  along the loading direction against the sample-level true stress ( $\sigma$ ) for several representative {hkl} reflections in the fcc and the bcc phases (see Supplementary Fig. 11 for  $\epsilon_{hkl}$  along the transverse direction against  $\sigma$ ). On the basis of these neutron-diffraction data, we calibrated our DP-CPFE model in terms of simulated lattice-strain responses (solid lines in Fig. 3a) that closely matched experimental measurements (symbols). Importantly, the

calibrated DP-CPFE model enables us to unravel the effects of stress partition and load transfer on the co-deforming fcc and bcc phases in nanolamellar eutectic colonies during their progressive yielding and hardening.

More specifically, we analysed the progressive yielding and hardening behaviour of fcc and bcc phases in nanolamellar eutectic colonies by dividing their lattice-strain responses into three stages (as marked in Fig. 3a). In stage I ( $\sigma < 1,100$  MPa), all crystallographic reflections in the fcc and the bcc phases underwent elastic deformation. The slope of each  $\sigma$ - $\varepsilon_{hkl}$  curve, known as the diffraction elastic constant  $E_{hkl}$ , varied among different reflections, owing to the elastic anisotropy of single-crystalline nanolamellae<sup>29,30</sup>. In stage II ( $\sigma \approx 1,100$ – $1,300$  MPa), crystallographic families in the fcc phase underwent progressive yielding, whereas those in the bcc phase remained elastic. Among the four representative fcc reflections in stage II, the {220} lattice strain along the loading direction first deviated from linearity and turned upwards; such a softening response indicates the onset of plastic yielding of this reflection. Meanwhile, the {200} lattice strain along the loading direction also deviated from linearity but turned downwards. Such a stiffening response arose primarily from load shedding from the plastic {220} to the elastic {200} reflections, as verified by DP-CPFE simulations. As  $\sigma$  increased, progressive yielding occurred sequentially from the {111}, {311} to {200} reflections, leading to their nonlinear lattice-strain responses. By contrast, among the three bcc crystallographic reflections of {110}, {211} and {321} in stage II, their lattice-strain responses remained linear, but the corresponding slope of each  $\sigma$ - $\varepsilon_{hkl}$  curve changed relative to stage I, indicating load transfer from progressively yielded fcc reflections to elastic bcc reflections. This load-partitioning behaviour of the AM lamellar EHEA differs from that of lamellar pearlitic steels where the bcc ferrite first yields and then transfers load to the orthorhombic cementite<sup>31–34</sup>. In stage III ( $\sigma > 1,300$  MPa), crystallographic families in the bcc phase became plastic, such that all crystallographic reflections of the fcc and the bcc phases in the nanolamellar eutectic colonies exhibited nonlinear lattice-strain responses.

We used DP-CPFE simulations to solve an inverse problem for determining the anisotropic elastic constants of individual fcc and bcc phases (Supplementary Section 6). As a result, the predicted lattice-strain responses (Fig. 3a) and sample-level stress–strain curve (Fig. 3b) from DP-CPFE simulations closely matched the experimental data. We further used DP-CPFE simulations to determine the average stress–strain responses of the fcc and the bcc phases in nanolamellar eutectic colonies (Fig. 3b). It is seen that both bcc and fcc nanolamellae exhibit high strengths and particularly high strain-hardening rates under the applied tensile strain up to about 14%. Notably, the bcc nanolamellae make greater contributions to the overall high strain-hardening responses than the fcc nanolamellae, thereby promoting the high tensile ductility of the present EHEA. Hence, the AM EHEA enables a high strain-hardening behaviour of bcc nanolamellae in eutectic colonies that is difficult to achieve in traditional bcc nanostructures<sup>31–33,35,36</sup>.

To investigate the deformation mechanisms, we analysed the dynamic evolution of dislocation densities from neutron-diffraction measurements. Figure 3c shows in situ neutron-diffraction spectra along the loading direction for the as-printed EHEA deformed to different strain levels. As shown in Fig. 3d and Supplementary Table 3,  $\rho_{\text{fcc}}$  first increased slowly from  $5.4 \times 10^{14} \text{ m}^{-2}$  in the as-printed state to  $7.9 \times 10^{14} \text{ m}^{-2}$  at 5% strain, and then increased more rapidly to  $1.3 \times 10^{15} \text{ m}^{-2}$  at 15% strain. In contrast,  $\rho_{\text{bcc}}$  had a higher initial value of  $7.4 \times 10^{14} \text{ m}^{-2}$  in the as-printed state, increased faster with increasing strain than  $\rho_{\text{fcc}}$ , and reached  $1.8 \times 10^{15} \text{ m}^{-2}$  at 5% strain and  $2.9 \times 10^{15} \text{ m}^{-2}$  at 15% strain. The faster increase of  $\rho_{\text{bcc}}$  is well correlated with the higher strain-hardening rate of bcc as opposed to fcc nanolamellae (Fig. 3b).

We used PED to characterize the dislocation evolution at different applied tensile strains (Fig. 4a–c and Supplementary Fig. 7). In the as-printed state, high densities of pre-existing dislocations were observed in both bcc and fcc nanolamellae with  $\rho_{\text{bcc}} \approx (7.4 \pm 1.1) \times 10^{14} \text{ m}^{-2}$

and  $\rho_{\text{fcc}} \approx (5.4 \pm 0.3) \times 10^{14} \text{ m}^{-2}$  (Fig. 4a). The high density of printing-induced dislocations is common for AM metals and is probably rooted in large thermal stresses developed during printing<sup>6</sup>. As the strain increased to 5%, more extensive dislocation multiplication was observed in bcc than in fcc nanolamellae (Fig. 4b), consistent with the neutron-diffraction measurements (Fig. 3d). The dislocations tended to aggregate at the lamellar interfaces, as evidenced by the strain contrast arising from highly defective fcc/bcc interfaces (Fig. 4b,e). This observation suggests that the lamellar interfaces serve as barriers and sinks for dislocations. The dislocations within the bcc nanolamellae are of mixed character, indicated by their curved line morphology (Fig. 4a–f). This morphology contrasts with the typical straight screw dislocations in bulk bcc metals<sup>37</sup>. The more isotropic glide behaviour of dislocations in bcc nanolamellae is attributed to the high operative stresses, and can stimulate more uniform deformation and thus offer steady strain hardening for bcc nanolamellae<sup>38,39</sup>. In addition, deformation-induced stacking faults were activated in the fcc nanolamellae (Fig. 4e and Extended Data Fig. 6), where the critical shear stress for nucleation of full dislocations could become high enough so that partial dislocations and thus stacking faults would increasingly prevail over full dislocations with increasing strain<sup>40</sup>. At a strain of about 15%, both bcc and fcc nanolamellae contained profuse dislocations (Fig. 4c,f), consistent with our in situ neutron-diffraction measurements. Furthermore, the nanometre-resolution inverse-pole figure (IPF) mapping confirmed the persistent Kurdjumov–Sachs orientation relationship between the two phases during deformation (Supplementary Fig. 7), which is often conducive to slip transmission across the semi-coherent phase interfaces.

We investigated the nanolamellar interfaces under HRTEM (Fig. 4g–i). The edge dislocation density at the interface and in its vicinity was low in the as-printed state, as shown in the inverse FFT (IFFT) micrograph using the  $(111)_{\text{fcc}}/(110)_{\text{bcc}}$  diffraction spots (Fig. 4j). As the strain level increased, more edge dislocations were observed at the interfaces whereas the dislocation density in the fcc and the bcc nanolamellae did not appear to increase dramatically (Fig. 4h,k). This observation provides evidence of effective dislocation storage at the phase interfaces. With further straining, more edge dislocations were observed not only at the interfaces but also within the nanolamellae, especially in the bcc phase (Fig. 4i,l). This trend suggests that the dislocation storage capability of the phase interfaces became increasingly saturated, thus promoting dislocation accumulation within the nanolamellae. Overall, the nanolamellar interfaces can effectively block and store dislocations, contributing to the excellent combination of high strength and high work hardening in our AM EHEA.

The high strain-hardening behaviour of the bcc nanolamellae in our AM EHEA contrasts with traditional nanocrystalline bcc metals that are strong but have low ductility because of a limited ability to accumulate intragranular dislocations for work hardening<sup>35,36</sup>. In the present AM EHEA, the fcc nanolamellae, in conjunction with the semi-coherent phase interfaces, could impose strong confinement on plastic straining of the bcc nanolamellae, thereby stabilizing their plastic flow with increasing strain. However, the strain compatibility requirement between microscale eutectic colonies can provide constraints at another level of structural hierarchy to promote work hardening in the bcc nanolamellae. This is because neighbouring colonies of different crystallographic orientations together with colony boundaries could not only limit dislocation glide through nanolamellae to individual colonies but also increase the resistance to plastic slip propagation to neighbouring colonies. As corroborated by DP-CPFE simulations, it is essential to account for such mutual constraints between microscale colonies to match the predicted lattice-strain responses with experimental measurements (Fig. 3a). Moreover, the printing-induced nanoscale compositional modulation in bcc nanolamellae (Fig. 1g,h) could further increase strain hardening to promote stable plastic flow of the bcc nanolamellae<sup>41–44</sup>. As chemical modulation in our EHEA occurs

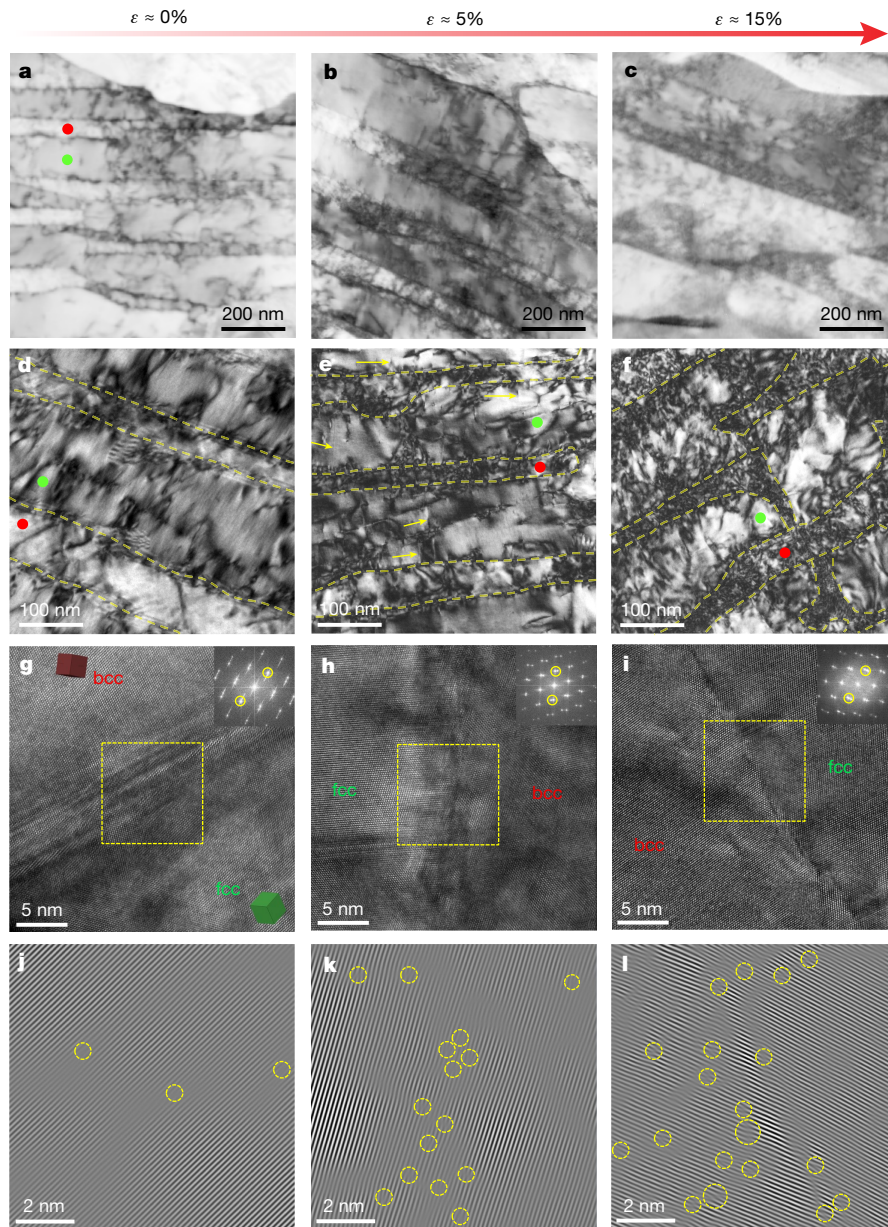


**Fig. 4 | Meso- and atomic-scale deformation structures.** **a–c**, Virtual bright-field PED micrographs revealing the evolution of dislocation substructures in bcc (indicated by the red dot) and fcc (indicated by the green dot) nanolamellae at tensile strains of about 0% (**a**), 5% (**b**) and 15% (**c**). The advantage of PED over conventional dislocation imaging is the elimination of most dynamical effects, leading to a crisper dislocation contrast. **d–f**, High-magnification bright-field TEM micrographs of the deformation substructures at tensile strains of about 0% (**d**), 5% (**e**) and 15% (**f**). Deformation-induced stacking faults, highlighted by

yellow arrows, were observed in fcc nanolamellae at 5% strain. The phase interfaces are indicated by the yellow dashed lines. **g–i**, HRTEM micrographs showing the atomic-level bcc and fcc phase interface at tensile strains of about 0% (**g**), 5% (**h**) and 15% (**i**), along with the FFT patterns (insets). **j–l**, IFFT micrographs for the yellow boxed regions in **g–i**, respectively. It is noted that the IFFT patterns reveal only the edge components of dislocations (highlighted by the yellow dashed circles) by showing extra half lattice planes, but the screw components are not readily visible.

over a larger length scale than that in random solid solutions, the ruggedness of the energy landscape controlling dislocation mobility becomes heightened, making dislocation motion more sluggish in bcc nanolamellae, as revealed by in situ TEM straining experiments (Supplementary Section 7). Therefore, the nanoscale compositional modulation in bcc nanolamellae can enhance the resistance to dislocation glide, leading to stronger dislocation interactions and more isotropic dislocation glide to promote the hardening responses<sup>28</sup>.

An important benefit of heterogeneous nanolamellar structures from L-PBF is the generation of large local plastic strain gradients leading to strong back-stress hardening<sup>45</sup>. As shown by in situ lattice-strain

measurements (Fig. 3a), plastic yielding initiated in the fcc phase whereas the bcc phase remained elastic. Geometric constraints from the elastic bcc phase could result in strong local plastic strain gradients near the lamellar interfaces, which would be accommodated by geometrically necessary dislocations (GNDs)<sup>45</sup>. Moreover, after the bcc phase became plastically yielded, additional deformation incompatibility between the two co-deforming phases arose from their plastic anisotropy (that is, different orientations and resistances of fcc and bcc slip systems) and would be accommodated by GNDs as well. Hence, continued build-up of GNDs near the fcc/bcc interfaces, in line with the HRTEM observations of increased interface dislocations with loading,

could generate strong back stresses<sup>46</sup> and thus elevate flow stresses of the AMEHEA. Extended Data Fig. 7 shows a typical loading–unloading–reloading curve with pronounced hysteresis loops that are indicative of a notable Bauschinger effect<sup>24</sup>, with the strong back stresses increasing from about 0.9 GPa to about 1.1 GPa with loading<sup>47</sup>. Hence, such strong back-stress hardening reflects the beneficial effect of heterogeneous nanolamellar structures from L-PBF, in contrast to the back-stress hardening through nanoprecipitates in the microlamellar EHEA from traditional thermomechanical treatment<sup>24</sup>.

In summary, we have harnessed additive manufacturing by L-PBF and the favourable compositional effects of EHEAs to develop a class of dual-phase nanolamellar alloys that exhibit an exceptional combination of high yield strength and high tensile ductility, which surpass those of other state-of-the-art AM alloys. The hierarchical, dual-phase nanostructure motif can be generally applied to other EHEA systems to improve their mechanical properties (Extended Data Fig. 8 for  $\text{Ni}_{40}\text{Co}_{20}\text{Fe}_{10}\text{Cr}_{10}\text{Al}_{18}\text{W}_2$  (ref. 48)). Mechanistic insights gained into the strengthening and hardening behaviour of AMEHEAs may be applied to the design of high-performance metal alloys that develop a rich variety of complex multi-phase lamellar structures such as aluminium alloys<sup>49</sup> and titanium alloys<sup>50</sup>.

## Online content

Any methods, additional references, Nature Research reporting summaries, source data, extended data, supplementary information, acknowledgements, peer review information; details of author contributions and competing interests; and statements of data and code availability are available at <https://doi.org/10.1038/s41586-022-04914-8>.

- DebRoy, T., Mukherjee, T., Wei, H. L., Elmer, J. W. & Milewski, J. O. Metallurgy, mechanistic models and machine learning in metal printing. *Nat. Rev. Mater.* **6**, 48–68 (2021).
- Martin, J. H. et al. 3D printing of high-strength aluminium alloys. *Nature* **549**, 365–369 (2017).
- Zhang, D. et al. Additive manufacturing of ultrafine-grained high-strength titanium alloys. *Nature* **576**, 91–95 (2019).
- Pham, M.-S., Liu, C., Todd, I. & Lertthanasarn, J. Damage-tolerant architected materials inspired by crystal microstructure. *Nature* **565**, 305–311 (2019).
- Kürnsteiner, P. et al. High-strength Damascus steel by additive manufacturing. *Nature* **582**, 515–519 (2020).
- Wang, Y. M. et al. Additively manufactured hierarchical stainless steels with high strength and ductility. *Nat. Mater.* **17**, 63–71 (2018).
- Cunningham, R. et al. Keyhole threshold and morphology in laser melting revealed by ultrahigh-speed X-ray imaging. *Science* **363**, 849–852 (2019).
- Todaro, C. J. et al. Grain structure control during metal 3D printing by high-intensity ultrasound. *Nat. Commun.* **11**, 142 (2020).
- Murray, S. P. et al. A defect-resistant Co–Ni superalloy for 3D printing. *Nat. Commun.* **11**, 4975 (2020).
- Barriobero-Vila, P. et al. Peritectic titanium alloys for 3D printing. *Nat. Commun.* **9**, 3426 (2018).
- Brif, Y., Thomas, M. & Todd, I. The use of high-entropy alloys in additive manufacturing. *Scr. Mater.* **99**, 93–96 (2015).
- Jensen, J. K. et al. Characterization of the microstructure of the compositionally complex alloy  $\text{Al}_3\text{Mo}_{0.5}\text{Nb}_7\text{Ta}_{0.5}\text{Ti}_1\text{Zr}_1$ . *Scr. Mater.* **121**, 1–4 (2016).
- George, E. P., Raabe, D. & Ritchie, R. O. High-entropy alloys. *Nat. Rev. Mater.* **4**, 515–534 (2019).
- Lu, Y. et al. A promising new class of high-temperature alloys: eutectic high-entropy alloys. *Sci. Rep.* **4**, 6200 (2014).
- Zhu, Y. et al. Enabling stronger eutectic high-entropy alloys with larger ductility by 3D printed directional lamellae. *Addit. Manuf.* **39**, 101901 (2021).
- Shi, P. et al. Hierarchical crack buffering triples ductility in eutectic herringbone high-entropy alloys. *Science* **373**, 912–918 (2021).
- Zhu, Y. T. & Liao, X. Retaining ductility. *Nat. Mater.* **3**, 351–352 (2004).
- Zheng, S. et al. High-strength and thermally stable bulk nanolayered composites due to twin-induced interfaces. *Nat. Commun.* **4**, 1696 (2013).
- Cheng, Z., Zhou, H., Lu, Q., Gao, H. & Lu, L. Extra strengthening and work hardening in gradient nanotwinned metals. *Science* **362**, eaau1925 (2018).
- Fan, L. et al. Ultrahigh strength and ductility in newly developed materials with coherent nanolamellar architectures. *Nat. Commun.* **11**, 6240 (2020).
- Thomas, M., Baxter, G. J. & Todd, I. Normalised model-based processing diagrams for additive layer manufacture of engineering alloys. *Acta Mater.* **108**, 26–35 (2016).
- Pham, M.-S., Dovgvy, B., Hooper, P. A., Gourlay, C. M. & Piglione, A. The role of side-branching in microstructure development in laser powder-bed fusion. *Nat. Commun.* **11**, 749 (2020).
- Bhattacharjee, T. et al. Simultaneous strength–ductility enhancement of a nano-lamellar  $\text{AlCoCrFeNi}_{23}$  eutectic high entropy alloy by cryo-rolling and annealing. *Sci. Rep.* **8**, 3276 (2018).
- Shi, P. et al. Enhanced strength–ductility synergy in ultrafine-grained eutectic high-entropy alloys by inheriting microstructural lamellae. *Nat. Commun.* **10**, 489 (2019).
- Gao, X. et al. Microstructural origins of high strength and high ductility in an  $\text{AlCoCrFeNi}_{23}$  eutectic high-entropy alloy. *Acta Mater.* **141**, 59–66 (2017).
- Misra, A., Hirth, J. P. & Hoagland, R. G. Length-scale-dependent deformation mechanisms in incoherent metallic multilayered composites. *Acta Mater.* **53**, 4817–4824 (2005).
- Porter, D. A. & Easterling, K. E. *Phase Transformations in Metals and Alloys* (CRC, 1981).
- An, Z. et al. Spinodal-modulated solid solution delivers a strong and ductile refractory high-entropy alloy. *Mater. Horiz.* **8**, 948–955 (2021).
- Chen, W. et al. Microscale residual stresses in additively manufactured stainless steel. *Nat. Commun.* **10**, 4338 (2019).
- Naeem, M. et al. Cooperative deformation in high-entropy alloys at ultralow temperatures. *Sci. Adv.* **6**, eaax4002 (2020).
- Raabe, D. et al. Metallic composites processed via extreme deformation: toward the limits of strength in bulk materials. *MRS Bull.* **35**, 982–991 (2010).
- Wang, Y., Ohnuki, T., Tomota, Y., Harjo, S. & Ohmura, T. Multi-scaled heterogeneous deformation behavior of pearlite steel studied by in situ neutron diffraction. *Scr. Mater.* **140**, 45–49 (2017).
- Ghosh, P., Kormout, K. S., Lienert, U., Keckes, J. & Pippan, R. Deformation characteristics of ultrafine grained and nanocrystalline iron and pearlitic steel—an in situ synchrotron investigation. *Acta Mater.* **160**, 22–33 (2018).
- Bhadeshia, H. Cementite. *Int. Mater. Rev.* **65**, 1–27 (2020).
- Jia, D., Ramesh, K. T. & Ma, E. Effects of nanocrystalline and ultrafine grain sizes on constitutive behavior and shear bands in iron. *Acta Mater.* **51**, 3495–3509 (2003).
- Wei, Q., Jiao, T., Ramesh, K. T. & Ma, E. Nano-structured vanadium: processing and mechanical properties under quasi-static and dynamic compression. *Scr. Mater.* **50**, 359–364 (2004).
- Hull, D. & Bacon, D. J. *Introduction to Dislocations* (Butterworth-Heinemann, 2001).
- Wang, F. et al. Multiplicity of dislocation pathways in a refractory multiprincipal element alloy. *Science* **370**, 95–101 (2020).
- Lee, C. et al. Temperature dependence of elastic and plastic deformation behavior of a refractory high-entropy alloy. *Sci. Adv.* **6**, eaaz4748 (2020).
- Chen, M. et al. Deformation twinning in nanocrystalline aluminum. *Science* **300**, 1275–1277 (2003).
- Rao, S. I. et al. Atomistic simulations of dislocations in a model bcc multicomponent concentrated solid solution alloy. *Acta Mater.* **125**, 311–320 (2017).
- Lei, Z. et al. Enhanced strength and ductility in a high-entropy alloy via ordered oxygen complexes. *Nature* **563**, 546–550 (2018).
- Ding, Q. et al. Tuning element distribution, structure and properties by composition in high-entropy alloys. *Nature* **574**, 223–227 (2019).
- George, E. P., Curtin, W. A. & Tasan, C. C. High entropy alloys: a focused review of mechanical properties and deformation mechanisms. *Acta Mater.* **188**, 435–474 (2020).
- Zhu, Y. et al. Heterostructured materials: superior properties from hetero-zone interaction. *Mater. Res. Lett.* **9**, 1–31 (2021).
- Cheng, Z. et al. Unraveling the origin of extra strengthening in gradient nanotwinned metals. *Proc. Natl Acad. Sci. USA* **119**, e2116808119 (2022).
- Dickson, J., Boutin, J. & Handfield, L. A comparison of two simple methods for measuring cyclic internal and effective stresses. *Mater. Sci. Eng.* **64**, L7–L11 (1984).
- Wu, Q. et al. Uncovering the eutectics design by machine learning in the Al–Co–Cr–Fe–Ni high entropy system. *Acta Mater.* **182**, 278–286 (2020).
- Zimmermann, M., Carrard, M. & Kurz, W. Rapid solidification of Al–Cu eutectic alloy by laser remelting. *Acta Metall.* **37**, 3305–3313 (1989).
- Sharma, G., Ramanujan, R. V. & Tiwari, G. P. Instability mechanisms in lamellar microstructures. *Acta Mater.* **48**, 875–889 (2000).

**Publisher's note** Springer Nature remains neutral with regard to jurisdictional claims in published maps and institutional affiliations.

© The Author(s), under exclusive licence to Springer Nature Limited 2022

## Methods

### Materials fabrication

AlCoCrFeNi<sub>2.1</sub> EHEA samples were fabricated by a commercial M290 (EOS) L-PBF machine, which is equipped with a ytterbium-fibre laser with a maximum power of 400 W and a focal diameter of 100  $\mu\text{m}$ . Gas-atomized AlCoCrFeNi<sub>2.1</sub> EHEA powders with particle sizes ranging from 15  $\mu\text{m}$  to 53  $\mu\text{m}$  (mean value 35  $\mu\text{m}$ ) were used (Vilory Advanced Materials Technology). All samples were built in an argon environment with an oxygen concentration below 1,000 ppm. A 4140 alloy steel plate was used as the printing substrate, which was pre-heated to 80 °C to mitigate the build-up of thermal residual stresses. To optimize the printing of fully dense samples, we first built a high-throughput sample library of many cubes ( $7 \times 7 \times 7 \text{ mm}^3$ ) with different laser processing parameters. We used an AccuPyc II 1340 gas pycnometer (Micromeritics) to measure the density for the cube library and thus identify the optimal printing conditions. We selected the parameters that yield samples with a relative density higher than 99.5% to build rectangular plates of 35 mm (length)  $\times$  10 mm (width)  $\times$  2 mm (build height) for mechanical testing. The optimal laser processing conditions are listed in Supplementary Table 1. The in situ thermal cycling (also called intrinsic heat treatment) inherent to the repetitive additive manufacturing process was investigated by comparing microstructures of a single-track bead with the multi-layer bulk sample and octet lattice (Supplementary Section 8). To study the effect of post heat treatment on the mechanical properties of the AMEHEA, the as-printed samples were subsequently annealed at different conditions, including 600 °C for 5 h, 660 °C for 1 h, 700 °C for 1 h, 800 °C for 1 h, 800 °C for 1 h plus 600 °C for 1 h, 900 °C for 30 min plus 600 °C for 1 h and 1,000 °C for 1 h, which were implemented in a tube furnace at a heating rate of 5 °C min<sup>-1</sup> under an argon protective atmosphere followed by water quenching. The as-cast AlCoCrFeNi<sub>2.1</sub> sample was prepared by vacuum arc melting of commercially pure constituent elements (99.9 wt%) under high-purity argon protection. The alloy was re-melted at least five times for chemical homogeneity and then solidified in a water-cooled copper mould with dimensions of 80 mm (length)  $\times$  10 mm (width)  $\times$  2 mm (thickness).

### Composition analysis

Chemical compositions of the AlCoCrFeNi<sub>2.1</sub> feedstock powders and the as-printed samples were analysed by inductively coupled plasma mass spectroscopy for metallic elements and instrumental gas analysis for non-metallic light elements, including oxygen and nitrogen.

### Mechanical testing

Dogbone-shaped tension specimens with a nominal gauge dimension of 8 mm (length)  $\times$  2 mm (width)  $\times$  1 mm (thickness) were cut from the rectangular plates by electrical discharge machining and finally polished to a metallurgical grit of 1200 silicon carbide paper. Quasi-static uniaxial tension tests were performed on an Instron 5969 universal testing machine at a strain rate of  $2 \times 10^{-4} \text{ s}^{-1}$ . The strain was measured by an Instron non-contact AVE2 video extensometer with a displacement resolution of 0.5  $\mu\text{m}$ . The tests were repeated two to three times for each type of sample. The back-stress evolution was measured through the loading–unloading–reloading test. Upon loading to each specific strain level at a strain rate of  $2 \times 10^{-4} \text{ s}^{-1}$ , the specimen was unloaded to 30 N under a force control mode with a rate of 200 N min<sup>-1</sup>, followed by reloading at a strain rate of  $2 \times 10^{-4} \text{ s}^{-1}$ .

### Neutron diffraction

In situ neutron-diffraction tensile tests were conducted at the beamline 7 engineering materials diffractometer, VULCAN<sup>51,52</sup>, at the Spallation Neutron Source, Oak Ridge National Laboratory. With the loading axis at 45° to the incident neutron beam, the time-of-flight neutron-diffraction data were collected simultaneously along the loading and transverse directions by two detector banks positioned at  $\pm 90^\circ$  to the incident

neutron beam. The dogbone-shaped tensile specimen with a nominal gauge dimension of 15 mm (length)  $\times$  2.6 mm (width)  $\times$  3 mm (thickness) was loaded with an MTS load-frame equipped with a contact extensometer to measure the strain. Strain control mode was employed for the loading cycles at a rate of  $2.8 \times 10^{-6} \text{ s}^{-1}$ , whereas force control mode was used for the unloading cycles at 2%, 5% and 10% engineering strains to quantify the dislocation density evolution at different strains more precisely by eliminating the effect of stress field on peak broadening. With a slit size of 8 mm (length)  $\times$  3 mm (width), the neutron-diffraction patterns were collected in a high-intensity mode with a lattice spacing resolution ( $\Delta d/d$ ) of about 0.45%. The neutron-diffraction data recorded during the continuous loading–unloading cycles were subsequently chopped at a time interval of 5 min. Single-peak fitting was performed by using the VDRIVE software<sup>53</sup>. The phase weight fraction was determined by full-pattern Rietveld refinement using the GSAS software<sup>54</sup>. The lattice strain for the  $\{hkl\}$  reflection,  $\varepsilon_{hkl}$ , was calculated by  $\varepsilon_{hkl} = (d_{hkl} - d_{0,hkl})/d_{0,hkl}$ , where  $d_{hkl}$  and  $d_{0,hkl}$  denote the interplanar spacings of  $\{hkl\}$  planes under loading and in the ‘stress free’ state (Supplementary Section 3), respectively. It is noted that neutron-diffraction measurements directly separate the lattice-strain responses from fcc and bcc phases in the  $\{hkl\}$  crystallographic family, thus facilitating the stress-partition analysis in dual phases. Residual lattice strains and intergranular residual stresses were also studied in the as-printed EHEA (Supplementary Section 3).

Pole figures of as-printed and fractured samples were also measured by neutron diffraction at VULCAN, which required the axial direction of the sample to rotate from the original  $-45^\circ$  to  $0^\circ$  off the incident beam direction by a step size of  $5^\circ$ . Following each step, the sample was rotated with respect to the current axial direction from  $0^\circ$  to  $360^\circ$  by a step size of  $30^\circ$ . After each step of rotation, neutron-diffraction data were collected for 2 min, and in total 120 measurements were performed for each sample. The integral intensities of different peaks were extracted from the diffraction patterns by single-peak fitting to generate the complete pole figures.

### Microstructure characterization

TEM specimens were first mechanically polished to about 100  $\mu\text{m}$  in thickness, then punched into 3-mm-diameter disks. These disks were twin-jet electropolished using a Tenupol-5 polishing system with a solution of 5% perchloric acid, 35% butanol and 60% methanol at  $-40^\circ\text{C}$ . All the specimens were first examined inside an FEI Tecnai TEM operating at 200 KeV. To better illuminate dislocations inside the AMEHEAs, both bcc and fcc phases were tilted to the zone axes ( $[011]_{\text{fcc}}$  and  $[\bar{1}11]_{\text{bcc}}$ ) and imaged using PED with a  $0.3^\circ$  precession angle and a 3-nm step size. The advantage of PED over conventional dislocation imaging is the elimination of most dynamical effects, leading to a crisper dislocation contrast. Moreover, phase and orientation can be identified in each pixel by comparing the diffraction patterns with the database. HRTEM and HAADF-STEM observations were conducted on an FEI Titan S/TEM operating at 300 KeV to trace the evolutions of phase interfaces at the atomic level. EDX analyses were performed on HAADF-STEM to quantify the compositions of the bcc and the fcc phases. The optical microscopy, SEM and electron backscatter diffraction (EBSD) samples were mechanically polished down to 20-nm surface roughness. The optical microscopy and SEM samples were further etched in a solution of nitric acid, hydrochloric acid and ethanol with a ratio of 1:3:8. Optical micrographs were acquired using the Olympus BX53M optical microscope under the differential interference contrast mode to also capture the micro-pore distribution and quantify the melt pool dimensions. SEM observations were performed on an FEI Magellan 400 instrument. EBSD mapping was carried out using a Tescan FERA SEM equipped with an EBSD detector from the Oxford Instrument with a 20-kV acceleration voltage and a 100-nm step size.

APT specimens were prepared using a Thermo Fisher Nova 200 dual-beam focused ion beam/SEM. A triangular prism wedge was lifted



# Article

out, sectioned, mounted onto silicon microtip array posts, sharpened using a 30-kV Ga<sup>+</sup> ion beam and cleaned using a 2-kV ion beam. The APT experiments were run using a CAMECA LEAP 4000XHR in laser mode with a 30-K base temperature, 60-pJ laser energy, a 0.5% detection rate and a 200-kHz pulse repetition rate. The APT results were reconstructed and analysed using CAMECA's interactive visualization and analysis software (IVAS 3.8).

## Effects of dual-phase nanolamellar structure on yield strength

The Hall–Petch relationship is used to estimate the lamellae size dependence of yield strength by considering dislocation pile-up against the phase interface<sup>26</sup>. The local stress acting on the leading dislocation in a pile-up is the applied shear stress  $\tau$  magnified by a factor of  $n$  being the number of pile-up dislocations. Plastic yielding occurs when this local stress reaches a critical stress  $\tau^*$ , leading to slip transmission across the phase interface. In general, these shear stresses are related to the Hall–Petch equation according to

$$\tau = \frac{\tau^*}{n} = k_0(\lambda_{\text{fcc}})^{-1/2}$$

where  $k_0$  is the strengthening coefficient and the relatively small lattice friction term is ignored. Our TEM analysis of the deformed sample at 5% strain showed an average number of pile-up dislocations of  $n \approx 5$ , which can be used to estimate the critical applied shear stress  $\tau$  upon plastic yielding as<sup>20</sup>

$$n = \frac{4\tau L}{Gb}$$

where  $L$  is the pile-up length and taken as half of the average thickness of fcc lamellae,  $G$  is the shear modulus ( $G_{\text{fcc}} = 81$  GPa, derived from our DP-CPFE modelling) and  $b$  is the Burgers vector length ( $b_{\text{fcc}} = 0.254$  nm, measured by neutron diffraction). Hence, we estimated the critical applied shear stress of dislocation slip transmission through the interface as  $\tau \approx 340$  MPa. Using the Taylor factor of the fcc phase (3.09, measured by EBSD), we estimated the tensile yield stress of the present EHEA as about 1 GPa, accounting for about 75% of the measured yield strength. This analysis indicates that the confinement from nanolamellae makes a predominant contribution to the high yield strength of the as-printed EHEA.

The high density of printing-induced dislocations in the bcc and fcc nanolamellae also makes an important contribution to the high yield strength of the as-printed EHEA. We estimated this strengthening effect using the Taylor hardening law<sup>55</sup>:

$$\Delta\sigma_d = M\alpha Gbp^{1/2}$$

where  $M$  is the Taylor factor (3.09 for the fcc phase and 2.71 for the bcc phase, measured from EBSD),  $\alpha$  is the dimensionless pre-factor (about 0.2 for the fcc phase<sup>56</sup> and about 0.24 for the bcc phase<sup>57</sup>),  $G$  is the shear modulus (81 GPa for the fcc phase and 57 GPa for the bcc phase, derived from our DP-CPFE modelling),  $b$  is the Burgers vector length (0.254 nm for the fcc phase and 0.248 nm for the bcc phase, measured by neutron diffraction) and  $\rho$  is the pre-existing dislocation density ( $(5.4 \pm 0.3) \times 10^{14} \text{ m}^{-2}$  for the fcc phase and  $(7.4 \pm 1.1) \times 10^{14} \text{ m}^{-2}$  for the bcc phase). The strengthening effect by pre-existing dislocations was estimated through the rule of mixture of the respective contribution from the fcc and bcc phases, giving a total increase of yield

strength of 280 MPa. Therefore, the combined strengthening effects from the nanolamellar structure and the printing-induced dislocations give an estimated yield strength of about 1,300 MPa, which is in good agreement with the measured yield strength.

## Data availability

The data of this study are included in the article, the Extended Data and the Supplementary Information.

## Code availability

The code used for finite-element analyses is publicly available on the GitHub repository at <https://github.com/yzhang951/CPFEM-VUMAT/tree/main/AM-HEA>.

51. An, K. et al. First in situ lattice strains measurements under load at VULCAN. *Metall. Mater. Trans. A* **42**, 95–99 (2011).
52. An, K., Chen, Y. & Stoica, A. D. VULCAN: a “hammer” for high-temperature materials research. *MRS Bull.* **44**, 878–885 (2019).
53. An, K. *VDRIVE: Data Reduction and Interactive Visualization Software for Event Mode Neutron Diffraction* ORNL Report No. ORNL-TM-2012-621 (Oak Ridge National Laboratory, 2012).
54. Larson, A. C. & Von Dreele, R. B. *General Structure Analysis System (GSAS)* Report LAUR 86-748 (Los Alamos National Laboratory, 2004).
55. Courtney, T. H. *Mechanical Behavior of Materials* (Waveland, 2005).
56. He, J. Y. et al. A precipitation-hardened high-entropy alloy with outstanding tensile properties. *Acta Mater.* **102**, 187–196 (2016).
57. Zhang, X., Hansen, N., Godfrey, A. & Huang, X. Dislocation-based plasticity and strengthening mechanisms in sub-20 nm lamellar structures in pearlitic steel wire. *Acta Mater.* **114**, 176–183 (2016).

**Acknowledgements** We thank D. Follette, P. Hou, M. Wu, K. A. Beyer and M. J. Frost for their experimental assistance. W.C. acknowledges support from the US National Science Foundation (DMR-2004429) and UMass Amherst Faculty Startup Fund. T.Z. acknowledges support from the US National Science Foundation (DMR-1810720 and DMR-2004412). Y.M.W. acknowledges support from the US National Science Foundation (DMR-2104933). T.V. acknowledges support from the Laboratory Directed Research and Development (LDRD) programme (21-LW-027) at Lawrence Livermore National Laboratory (LLNL). His work was performed under the auspices of the US Department of Energy (DOE) by LLNL under contract no. DE-AC52-07NA27344. In situ neutron-diffraction work was carried out at the Spallation Neutron Source (SNS), which is a US DOE user facility at the Oak Ridge National Laboratory (ORNL), sponsored by the Scientific User Facilities Division, Office of Basic Energy Sciences. APT research was supported by the Center for Nanophase Materials Sciences (CNMS), which is a US DOE Office of Science User Facility at ORNL. We thank J. Burns for assistance in performing the APT sample preparation and running the APT experiments. This research also used high-energy X-ray resources of the Advanced Photon Source (Beamline 11-ID-C), a US DOE Office of Science User Facility operated at Argonne National Laboratory under contract number DE-AC02-06CH11357.

**Author contributions** J.R. and W.C. developed the three-dimensional printing-process map. J.R. and F.K. fabricated all samples and performed the processing parameters optimization. J.R., Y.L., L.L. and S.P. performed the optical microscopy and SEM microstructure characterization and mechanical testing. D.Z., K.Y.X., G.G., T.V. and Y.M.W. performed the EBSD and TEM characterization and analyses. J.R., Y.C., K.A. and W.C. conducted in situ neutron-diffraction experiments and analysed the data. J.D.P. collected and analysed the APT data. S.G. conducted the thermodynamic calculation. Y.Z. and T.Z. developed the DP-CPFE model and performed numerical simulations. J.R., Y.Z., D.Z., K.Y.X. T.Z. and W.C. drafted the initial manuscript. W.C. conceived, designed and led the project. All co-authors contributed to the data analysis and discussion.

**Competing interests** The authors declare no competing interests.

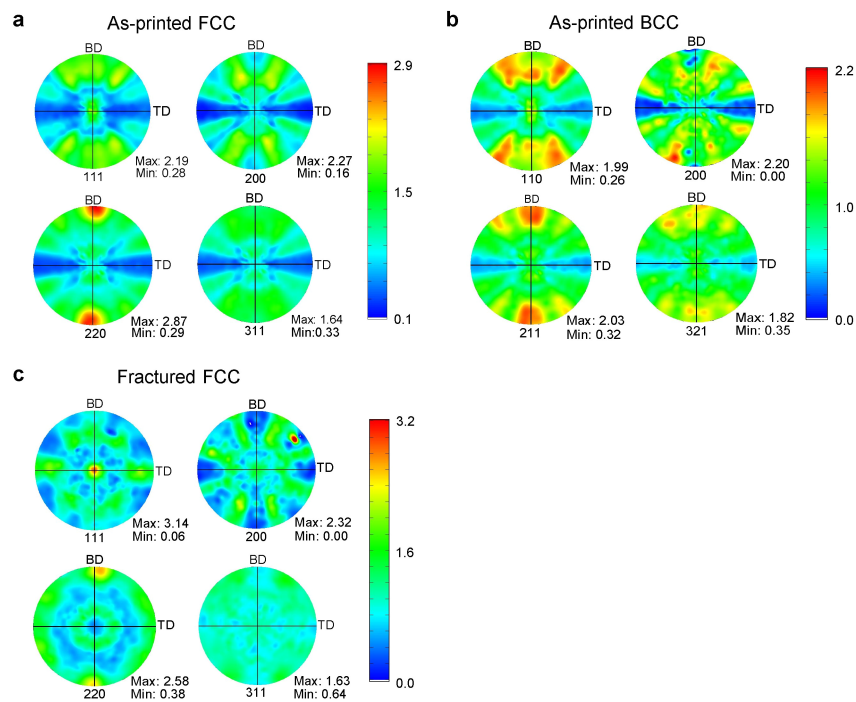
## Additional information

**Supplementary information** The online version contains supplementary material available at <https://doi.org/10.1038/s41586-022-04914-8>.

**Correspondence and requests for materials** should be addressed to Ting Zhu or Wen Chen.

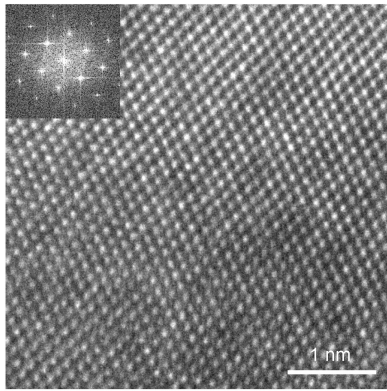
**Peer review information** *Nature* thanks Sheng Guo, Minh-Son Pham and the other, anonymous, reviewer(s) for their contribution to the peer review of this work.

**Reprints and permissions information** is available at <http://www.nature.com/reprints>.

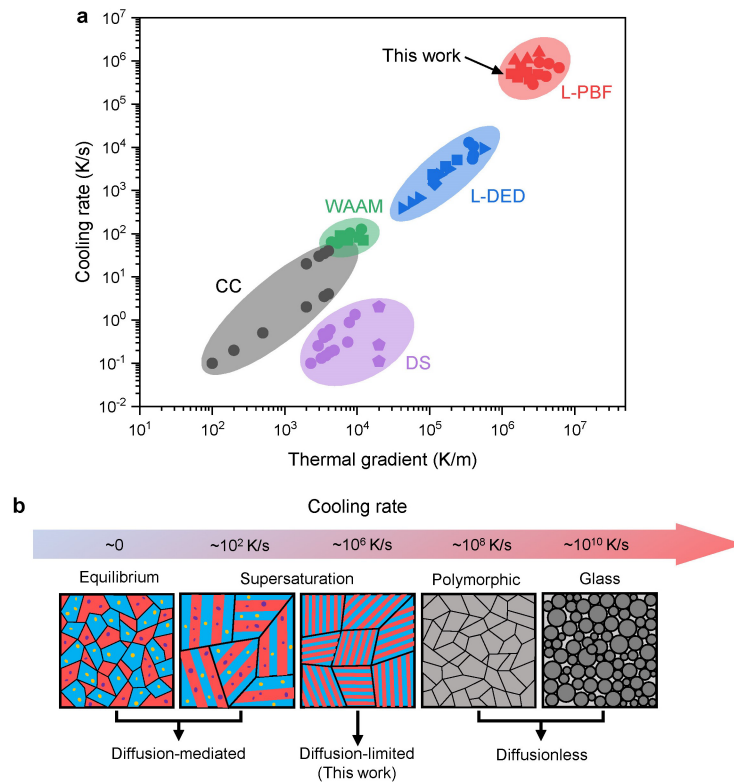


**Extended Data Fig. 1 | Pole figures of as-printed AlCoCrFeNi<sub>2.1</sub>, acquired by neutron diffraction. a,** Pole figures of FCC- (111), (200), (220), and (311) before loading. **b,** Pole figures of BCC-(110), (200), (211), and (321) before loading. **c,** Pole figures of FCC- (111), (200), (220), and (311) after fracture. Because the BCC peaks display extensive broadening after fracture, single-peak fittings are not convergent at lots of beam incident directions and pole figures of BCC orientations after fracture are not available. In all pole figures, the loading

direction (LD) is out of plane, the transverse direction (TD) is along the horizontal direction, and the build direction (BD) is along the vertical direction. Before loading, the as-printed sample shows a rather weak texture with slightly preferred orientation of FCC-(110)//BD. After fracture, the FCC-(111)//LD texture is developed, suggesting prominent dislocation slips on {111} planes in the FCC phase.

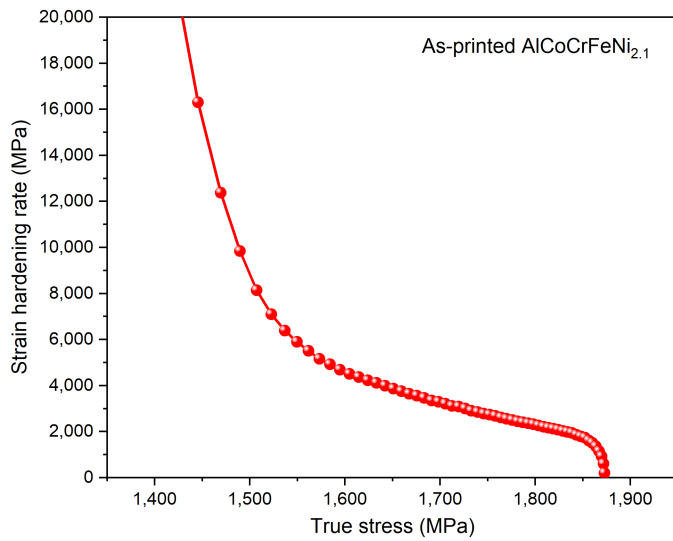


**Extended Data Fig. 2 | High-resolution TEM image showing the consistent crystal structure within BCC nanolamellae.** The inset shows the corresponding Fast Fourier Transform (FFT) diffractogram of the entire area that can provide chemical ordering information. No alternating intensity variation is observed in the FFT diffractogram, suggesting that no apparent ordered B2 phase is present.

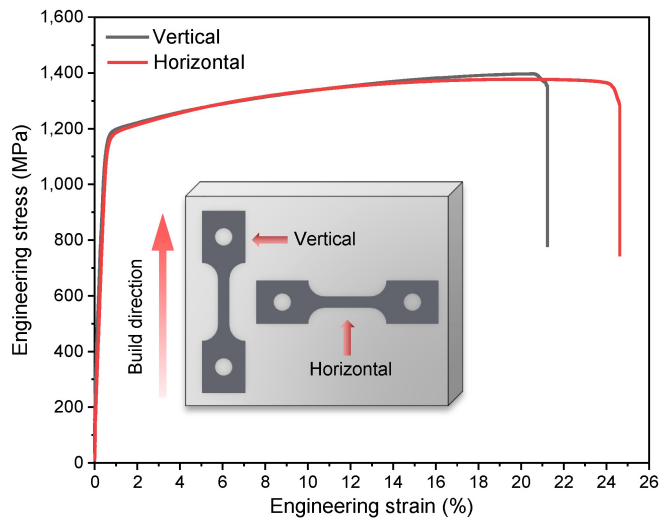


**Extended Data Fig. 3 | Extreme processing conditions enabled by L-PBF and the resulting highly metastable microstructure of multi-component eutectic alloys. a,** Comparison of cooling rate and thermal gradient between several additive manufacturing methods such as laser powder bed fusion (L-PBF) – used in this work, laser directed energy deposition (L-DED), wire arc additive manufacturing (WAAM), as well as conventional casting (CC) and

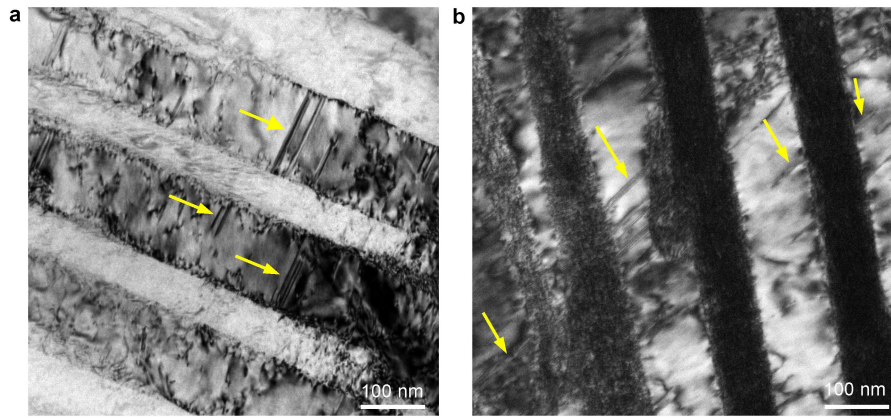
directional solidification (DS)<sup>1</sup>. Extremely large cooling rates and thermal gradients are inherent to the unique spatial-temporal feature of L-PBF and thus give rise to the diffusion-limited solidification and far-from-equilibrium microstructure of our EHEAs. **b,** Schematic illustration of the cooling rate effects on microstructural morphologies and length scales for typical dual-phase multi-component eutectic alloys.



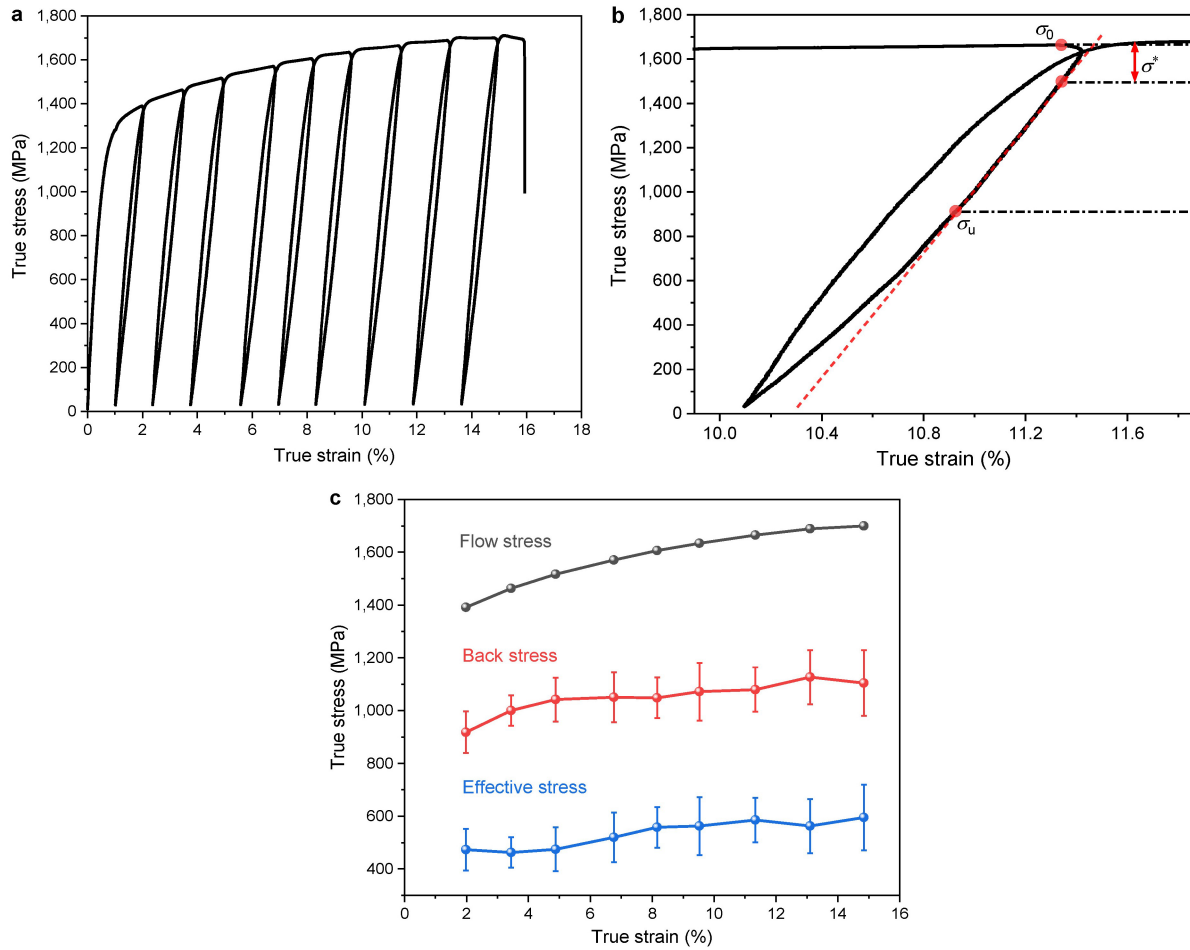
**Extended Data Fig. 4 | Kocks-Mecking plot showing the strain-hardening rate of as-printed AlCoCrFeNi<sub>2.1</sub>.** Strain-hardening rate (i.e., rate of increase of true stress with respect to true strain) is plotted as a function of true stress. Symbols represent experimental data points and the solid line is the fitting curve.



**Extended Data Fig. 5 | Tensile stress-strain curves of as-printed AlCoCrFeNi<sub>2.1</sub> EHEAs along different directions.** Comparable mechanical properties of these samples at a similar build height demonstrate the isotropic mechanical behaviour of AM AlCoCrFeNi<sub>2.1</sub> EHEA consisting of nanolamellar eutectic colonies with nearly random orientations.



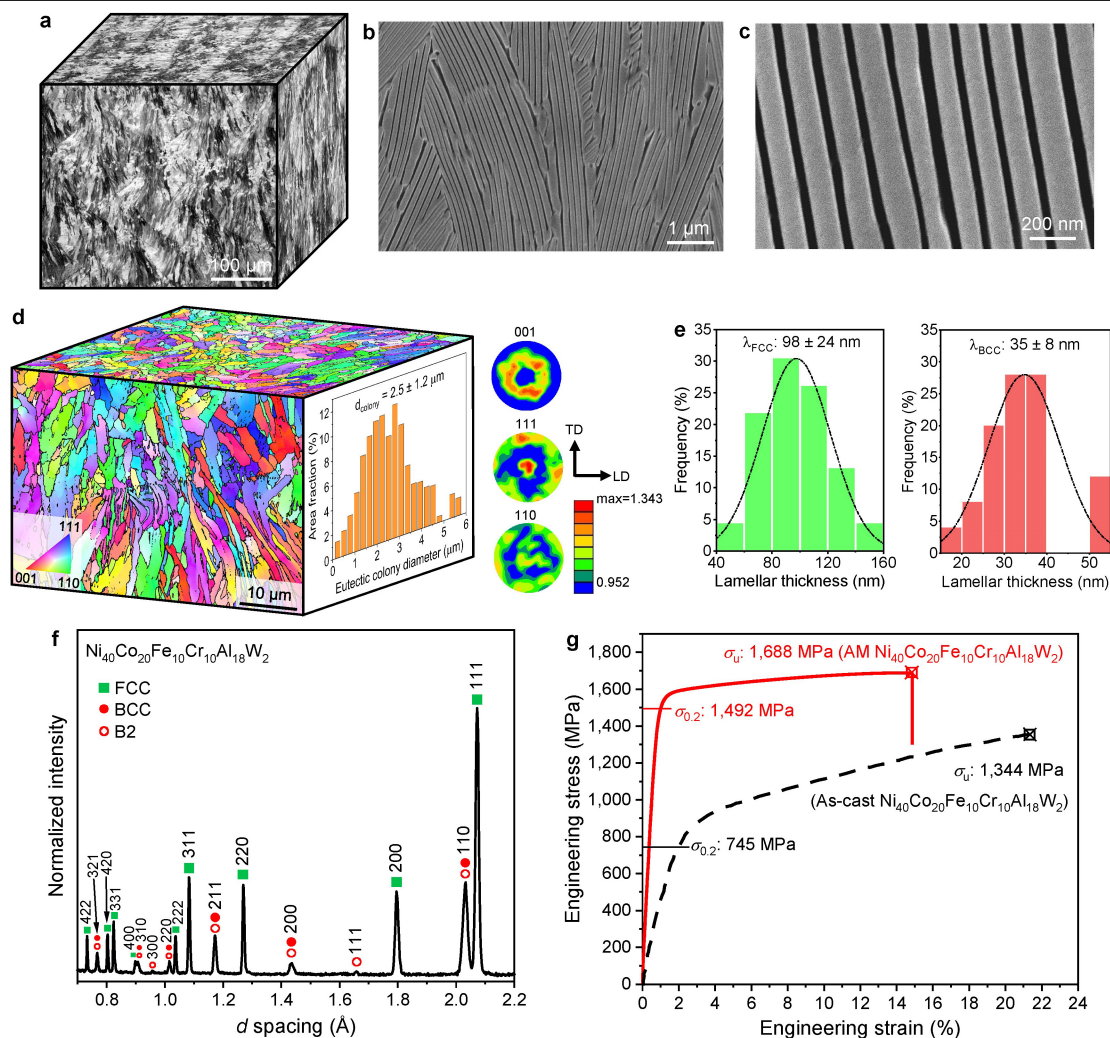
**Extended Data Fig. 6 | TEM images showing stacking faults (SFs) in strained FCC nanolamellae. a,** SFs observed at the strain level of 5%. **b,** Same as **a** except at 15%. SFs are highlighted by yellow arrows.



**Extended Data Fig. 7 | Evolution of backstress during tensile deformation of as-printed AlCoCrFeNi<sub>2.1</sub>.** **a**, Loading-unloading-reloading (LUR) true stress-strain curve. **b**, A representative LUR cycle showing the hysteresis loop. The back stress is calculated by Dickson's method and thus defined as

$\sigma_b = \sigma_0 - \sigma_e = (\sigma_0 + \sigma_u)/2 - \sigma^*/2$ , where  $\sigma_b$  denotes the back stress,  $\sigma_0$  the flow stress before unloading,  $\sigma_e$  the effective stress,  $\sigma_u$  the unloading yield stress, and  $\sigma^*$  the viscous stress. **c**, Flow stress, back stress, and effective stress versus true strain during tensile deformation. Error bars represent the standard deviation.





**Extended Data Fig. 8 | AM  $\text{Ni}_{40}\text{Co}_{20}\text{Fe}_{10}\text{Cr}_{10}\text{Al}_{18}\text{W}_2$  EHEA with high strength and large tensile ductility. a, 3D-reconstructed optical micrographs.**

**b**, Secondary electron micrograph showing the microscale eutectic colonies with different growth directions. **c**, Secondary electron micrograph revealing the typical nanolamellar structure. **d**, 3D-reconstructed EBSD IPF maps. The eutectic colony size distribution is obtained from the top-view map. The 001, 110, 111 pole figures of FCC phase are collected from the top-view EBSD map. Note that the BCC nanolamellae are difficult to index by EBSD due to their ultra-small thicknesses of  $\sim 35 \text{ nm}$ . **e**, Lamellar thickness distribution of BCC and FCC lamellae in as-printed  $\text{Ni}_{40}\text{Co}_{20}\text{Fe}_{10}\text{Cr}_{10}\text{Al}_{18}\text{W}_2$  EHEA. The average

interlamellar spacing ( $\lambda \approx 133 \text{ nm}$ ) is  $\sim 5$ -times smaller than that in the as-cast  $\text{Ni}_{40}\text{Co}_{20}\text{Fe}_{10}\text{Cr}_{10}\text{Al}_{18}\text{W}_2$  ( $\lambda \approx 0.82 \mu\text{m}$ ). **f**, Neutron-diffraction pattern of AM  $\text{Ni}_{40}\text{Co}_{20}\text{Fe}_{10}\text{Cr}_{10}\text{Al}_{18}\text{W}_2$  composed of FCC and BCC/B2 phases. **g**, Quasi-static tensile stress-strain curves of the as-cast and AM  $\text{Ni}_{40}\text{Co}_{20}\text{Fe}_{10}\text{Cr}_{10}\text{Al}_{18}\text{W}_2$  EHEAs. Our AM EHEA exhibits a high yield strength of  $\sim 1.5 \text{ GPa}$  and ultimate tensile strength of  $\sim 1.7 \text{ GPa}$ , which outperform the as-cast counterpart by twofold with no significant loss in ductility. Note that the tensile stress-strain curve of the as-cast sample (dashed line) is taken from the literature; the substantially low elastic modulus and large elastic strain limit are likely due to the inaccurate strain measurement of this literature result.

**Extended Data Table 1 | Compositions of FCC and BCC phases in as-printed AlCoCrFeNi<sub>2.1</sub>, compared with as-cast counterpart<sup>25</sup>**

Sample condition	Phase	Element (at%)				
		Al	Co	Cr	Fe	Ni
Nominal	Nominal	16.4	16.4	16.4	16.4	34.4
As-printed (this work)	FCC	12.8 ± 1.6	17.4 ± 0.6	17.9 ± 1.6	18.6 ± 1.0	33.0 ± 1.4
	BCC	21.3 ± 3.3	15.2 ± 0.9	14.2 ± 3.6	15.2 ± 1.7	33.8 ± 3.0
As-cast <sup>25</sup>	FCC(L1 <sub>2</sub> )	6.43 ± 0.02	21.14 ± 0.02	24.36 ± 0.02	24.16 ± 0.02	23.93 ± 0.02
	BCC(B2)	38.56 ± 0.01	10.12 ± 0.01	4.12 ± 0.01	9.20 ± 0.01	37.98 ± 0.01

These compositions are extracted from APT elemental distribution maps (Fig. 1h). Errors represent one standard deviation.